THE JOURNAL OF PHYSICAL CHEMISTRY A
A JOURNAL OF THE AMERICAN CHEMICAL SOCIETY

pubs.acs.org/JPCA

Article

Evaporation and Molecular Beam Scattering from a Flat Liquid Jet

Chin Lee,[#] Marvin N. Pohl,[#] Isaac A. Ramphal, Walt Yang, Bernd Winter, Bernd Abel, and Daniel M. Neumark*

Cite This: *J. Phys. Chem. A* 2022, 126, 3373−3383

Read Online

ACCESS | Metrics & More | Article Recommendations

ABSTRACT: An experimental setup for molecular beam scattering from flat liquid sheets has been developed, with the goal of studying reactions at gas−liquid interfaces for volatile liquids. Specifically, a crossed molecular beam instrument that can measure angular and translational energy distributions of scattered products has been adapted for liquid jet scattering. A microfluidic chip is used to create a stable flat liquid sheet inside vacuum from which scattering occurs, and both evaporation and scattering from this sheet are characterized using a rotatable mass spectrometer that can measure product time-of-flight distributions. This article describes the instrument and reports on the first measurements of evaporation of dodecane and Ne from a Ne-doped dodecane flat jet, as well as scattering of Ne from a flat jet of pure dodecane.

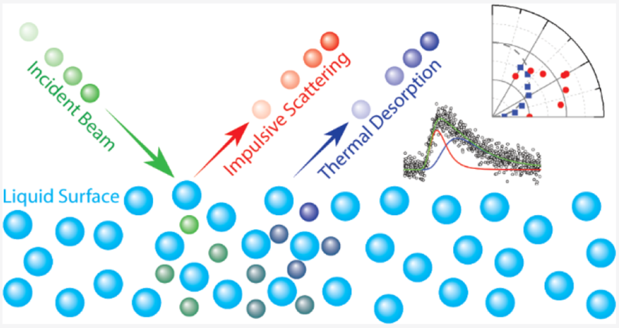

1. INTRODUCTION

The gas−liquid interface is a ubiquitous chemical environment in nature. It plays a major role in industrial processes, atmospheric chemistry, and environmental science. Examples include air−fuel mixing in internal combustion engines,[1] acid rain formation,[2−4] tropospheric aerosol surface chemistry,[5] and the uptake of CO_2 at the ocean−air interface, where about one-third of anthropogenically generated CO_2 is absorbed.[6] It is thus desirable to develop a molecular-scale understanding of chemistry at the gas−liquid interface.

Experiments employing an array of techniques have demonstrated that chemistry at the interface of a liquid solution can differ markedly from that in a bulk liquid or in the gas phase.[7−9] As examples, second harmonic and sum-frequency generation that rely on symmetry-breaking effects at the surface provide highly surface-specific spectroscopic information on species at the liquid interface.[10−12] X-ray photoelectron spectroscopy of liquid jets[13−16] and aerosols[17] probes solvent and solute molecules lying within 1−3 nm of the interface. Surface sampling of Langmuir troughs enables chemical analysis of photochemical products at the liquid interface and in the bulk.[18] Mass spectrometry-based experiments on thin films as well as droplets in microemulsions and the gas phase have shown significantly enhanced surface chemical reaction rates compared to that in bulk liquids.[19−21]

Molecular beam scattering, originally developed to probe interactions between pairs of gas-phase molecules[22,23] and gas-phase molecules with solid surfaces,[24,25] has proved to be a direct and powerful means for investigating the dynamics of elementary chemical reactions. Nathanson and others have shown that molecular beam scattering from liquids offers a unique probe of gas−liquid interfacial interactions.[26] Through this technique, two possible mechanisms are revealed—impulsive scattering (IS) and thermal desorption (TD). These mechanisms give rise to components with fast and slow velocity distributions, respectively. The TD signal represents gas molecules that undergo surface trapping upon impact with the liquid surface long enough for thermalization to occur prior to desorption. IS results from gas molecules that do not penetrate the liquid and experience negligible surface residence times (with respect to thermalization), recoiling elastically or losing only a fraction of their initial energy. They scatter preferentially into angles that depend sensitively on the initial energy and impact angle.[27] Note that IS and TD are limiting rather than clear-cut regimes for the scattering of molecules from liquids. Nonetheless, this dichotomy provides a useful framework for the interpretation of our results, and we use it as such throughout this work.

Molecular beam surface scattering experiments require compatibility with a vacuum environment and a clean sample surface, both of which are particularly challenging for liquid samples. Great advances were made by Fenn and co-workers in developing a robust technique that utilized rotating wheels to

Received: February 17, 2022
Revised: April 22, 2022
Published: May 17, 2022

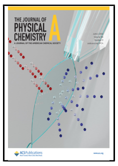

ACS Publications

https://doi.org/10.1021/acs.jpca.2c01174
J. Phys. Chem. A 2022, 126, 3373−3383

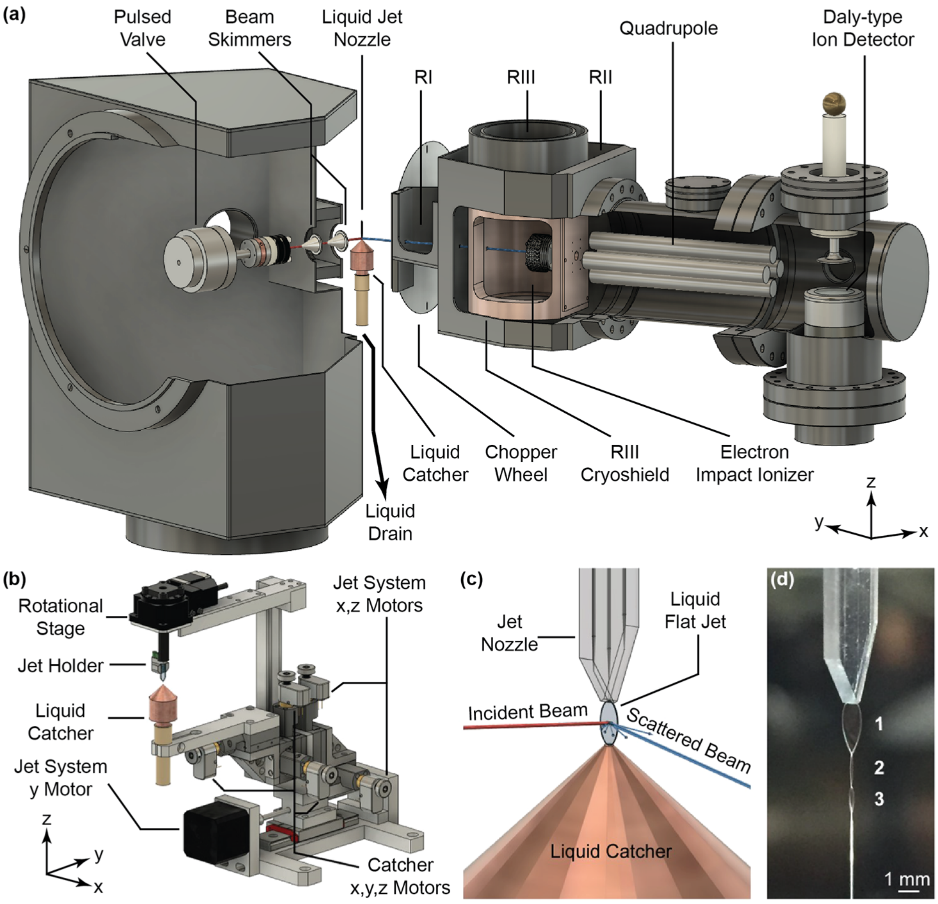

Figure 1. (a) Sectional view of scattering apparatus with crucial components highlighted. All components are situated inside the main chamber (not shown). The chamber on the left housing the pulsed valve is referred to as the source chamber, while the chamber on the right containing all detector components is referred to as the detector chamber. Lines indicate the molecular beam (red trace) striking the flat liquid jet surface and scattering off it (blue trace). Scattered molecules are then ionized, mass-selected, and subsequently collided onto a negatively charged high-voltage electrode. (b) Seven-axis jet holder system. Details are given in the main text. (c) Zoomed-in view of the jet-catcher assembly. The liquid catcher is carefully positioned at the first jet node of the flat jet to reduce the main chamber pressure. (d) Photograph of a stable dodecane flat jet at a 2.5 mL min^{-1} liquid flow rate, demonstrating the formation of multiple perpendicular liquid sheets. Under optimal conditions, several perpendicular liquid sheets can be produced.

generate continuously refreshed liquid films.[28,29] This "wetted wheel" approach was later used by Nathanson, Minton, and others to perform molecular scattering experiments in low-vapor-pressure systems ($<10^{-3}$ Torr) including long-chain hydrocarbons,[30] glycerol,[31] ionic liquids,[32] salty water at 212 K,[33] and perfluoropolyether.[34]

In order to carry out experiments on more volatile liquids, Faubel and co-workers developed micrometer-thin cylindrical water jets.[35,36] They showed that the small size and curvature of these jets greatly lowers the vapor density above the surface, thus reducing gas-phase collisions between evaporating particles. In 2013, Nathanson used the liquid jet technique for gas−liquid scattering experiments[37] and was able to study molecular beam scattering from liquid water and other volatile liquids. These included collisions of DCl molecules with salty water at 238 K,[38] scattering of Ne and O_2 from liquid dodecane,[37] collisions of Cl_2 and N_2O_5 with surfactant-coated Br^--glycerol solutions,[39,40] and collisions of organic molecules with salty water.[41]

Despite the access to higher-vapor-pressure liquids provided by the cylindrical microjet, its geometry is not particularly well-suited for scattering experiments. A cylindrical jet provides a much smaller scattering target than a wetted wheel; its typical diameter of 15−30 μm is considerably smaller than the usual dimensions of molecular beams (~1 mm). Moreover, the scattering angle from a cylindrical jet is not well-defined, making it challenging to measure product angular distributions, a central attribute of scattering experiments.

We herein present a novel approach of producing millimeter-sized flat liquid sheets inside vacuum to facilitate gas−liquid scattering experiments with a more optimal scattering target. These so-called "flat jets" have been successfully used in various spectroscopy experiments.[42−46] The goal of this work is to extend the capabilities of scattering experiments to the surfaces of volatile liquid flat jets, enabling both the speed and angular distributions of escaping molecules to be determined. As such, the current work presents the first application of flat liquid jets in a scattering experiment. We focus here on the volatile liquid dodecane (P_{vap} = 1.5 × 10^{-2} Torr at 275 K), a key component of jet fuel surrogates,[47] to present current experimental capabilities.

Two types of experiments are carried out: evaporation and scattering. We explore the evaporation of Ne-doped dodecane solutions in order to isolate the trapping−desorption process, which is one of the major channels encountered in scattering experiments, and a detailed understanding of evaporation from a flat jet will be key to successfully interpreting scattering experiments. Additionally, evaporation provides the opportunity to evaluate the performance of our instrument as liquid evaporation from cylindrical jets has been extensively studied.[37] Molecular beam scattering experiments of Ne from a dodecane flat jet are also described, in which measurement of the scattered Ne velocity and angular distributions enables the elucidation of the IS and TD mechanisms.

2. EXPERIMENTAL SECTION

2.1. Instrument Design. The gas−liquid scattering apparatus consists of a modified crossed molecular beam machine described elsewhere in great detail.[48,49] The general layout is shown in Figure 1a. It consists of a source chamber where a molecular beam is produced, a main chamber where the beam interacts with the liquid jet, and a detector chamber that houses the ionization and detection components. All chambers are pumped using turbomolecular pumps. In the source chamber, a pulsed molecular beam is generated using a piezoelectric valve (MassSpecpecD BV, Enschede) operated at a 200 Hz repetition rate and a pulse duration of 20−30 μs [full width at half maximum (FWHM), measured 330 mm downstream from the valve orifice].[50,51] Stagnation conditions within the valve reservoir are typically 286 K and 3000 Torr, leading to supersonic expansion of the gas mix through a 500 μm orifice when the valve is opened. The beam expands for 40 mm before encountering a 1 mm diameter conical skimmer that separates the source and main chambers. After another 30 mm, the molecular beam passes through a second 1 mm collimation skimmer. Residual transverse velocity in the molecular beam leads to a beam size of 4 mm at the interaction region. With a flat jet width of around 1 mm (see the next section), some portion of the beam will miss the jet and can pass directly into the detector. This effect is most pronounced within 5° of the molecular beam axis (x-axis in Figure 1a,b); thus, we typically position the detector at least 20° from the beam axis to eliminate this contribution.

The main chamber is where the gas−liquid interactions take place. Using the translation mechanisms described below, a liquid jet is precisely positioned at the interaction region where the molecular beam and detector fields of view intersect. The detector chamber is housed within the main chamber and comprises an electron impact ionizer, a quadrupole mass filter, and ion detector components.[48] It consists of three differentially pumped regions and can be sealed from the main chamber using a gate valve, which opens to either a 100 μm diameter circular aperture or a 3 × 3 mm^2 square aperture. The small aperture is used for molecular beam velocity characterization, while the larger aperture is used for evaporation and scattering experiments in order to view the entire width of the flat jet.

Typical pressures in the main chamber range in the low to mid 10^{-6} Torr range depending on whether a dodecane jet is running or not. This low main chamber pressure during jet operation is achieved by installing a large copper panel cooled by a gravity-fed liquid nitrogen dewar. This cryogenic shield has an area of approximately 0.98 m^2. With a sticking coefficient for dodecane of essentially unity, similar to that of water, the pumping speed is estimated as ∼45,000 L s^{-1}.[52] The pressure reduction observed with the cryogenic shield is consistent with this factor of increase in pumping speed. The ionizer chamber pressure is in the low to mid 10^{-11} Torr range, achieved by a combination of three stages of differential pumping (regions RI−RIII) and liquid nitrogen cryogenic cooling.

The liquid jet must be aligned simultaneously with respect to a catcher that disposes the liquid waste and to the molecular beam and detector axes.[53] This is achieved via an array of piezoelectric stages that allow for independent control over the three translational dimensions of the catcher relative to the jet, as well as the entire jet−catcher assembly relative to the interaction region. The setup is shown in Figure 1b. The entire jet assembly is mounted on a precise stepper motor that can retract both the jet and catcher several centimeters away from the molecular beam axis, allowing direct characterization of the molecular beam prior to scattering experiments. In addition, the jet holder is mounted to a 360° rotation stage in order to vary the molecular beam incident angle, θ_i. The positions of the jet and catcher are monitored using two cameras equipped with zoom lenses.

For evaporation experiments, the molecular beam is shut off, and the liquid surface is positioned such that the surface normal (y-axis in Figure 1a,b) is perpendicular to the molecular beam axis. In this configuration, the detector can sweep through 0 to 90° with respect to the jet surface normal. For scattering experiments, the molecular beam is directed onto the liquid surface. While θ_i can be freely chosen, we are limited to detector positions for the scattering angles, θ_f, between $90° - \theta_i$ and 90°.

2.2. Liquid Jet Generation. Experiments have previously been carried out on flat jets formed by colliding two individual cylindrical jets,[42,44,54,55] but space limitations around the interaction region in our setup necessitate a more compact approach. The nozzle design routinely used in our lab is a microfluidic chip prepared by etching channels into borosilicate glass, developed by Micronit BV in collaboration with the SLAC National Accelerator Laboratory.[56] As shown in Figure 1c, the chip has three channels, where the central channel is connected to one inlet port, along with another inlet port that diverges into two outer channels that then reconverge at the nozzle exit. The central channel and outer channels have dimensions of 20 × 25 and 50 × 55 μm^2, respectively, with a 5 μm tolerance for each dimension. This nozzle was designed to operate as a gas dynamic virtual nozzle at SLAC, using high-pressure gas in the outer channels to compress liquid from the central channel into extremely thin sheets (<20 nm). Gas dynamic jet operation is obviously not compatible with a molecular scattering experiment. Instead, during operation in the colliding jet mode, liquid is pumped through the outer channels, while the central channel is left unused. Cylindrical jet operation is made possible by swapping the liquid inlet from the split outer channels to the single central channel. The dimensions of this channel lead to a cylindrical jet approximately 25 μm in diameter. Figure 1d shows a dodecane flat jet produced using this nozzle design with the colliding jet mode by pumping 2.5 mL min^{-1} of dodecane into the split outer channels.

Liquid is delivered to the jet nozzle through 1/16 in. PEEK tubing lines and pressurized using a high-performance liquid chromatography (HPLC) pump at flow rates between 0.5 and 3.5 mL min^{-1}, resulting in pressures between 10 and 70 bar depending on the in-line particulate filter pore size, jet nozzle, and liquid viscosity (determined by the liquid temperature and solvent identity). This translates to flow velocities between 1 and 10 m s^{-1}, which means that particles that stick onto the liquid surface must desorb within about 0.5−5 ms before they are carried out of view of the detector (~5 mm at the interaction region with a 3 × 3 mm^2 aperture). The fixed 80° collision angle of these commercially available nozzles conveniently produces jets with dimensions compatible with molecular beams. Typical dimensions are 1.7 × 5.1 mm^2 (W × H) flat sheets for dodecane at a 3.5 mL min^{-1} flow rate, bounded by a thicker fluid rim with a diameter of around 50 μm.[56] Before reaching the jet nozzle, the liquid passes through a counter-current heat exchanger to lower its temperature and thus reduce the vapor pressure of the liquid. The coolant in the heat exchanger is set to be close to the liquid's freezing point; for example, it is set to be −7 °C for dodecane, for which the freezing point is −9 °C. This heat exchanger is attached to the chamber such that its exit side is inside the vacuum and therefore minimizes possible heat transfer en route to the nozzle.

Often, cylindrical liquid jets in vacuum are collected by directing them onto a cryogenically cooled surface that freezes the liquid waste and stores it inside the vacuum chamber.[46,57] However, when using a flat jet with much higher flow rates, it is preferable to catch the jet 2−5 mm downstream with a small orifice placed at the sheet node.[42,53] Thus, only a small fraction of the jet is exposed to the vacuum, which drastically reduces the overall gas load in the chamber. We use a stainless-steel catcher with a 1 mm diameter orifice to collect the liquid jet. We have the additional capability to collect more volatile solvents in the future by installing a heated copper−beryllium catcher supplied by Microliquids GmbH (defunct, similar in design to the catcher produced by Advanced Microfluidic Systems GmbH, Göttingen). The bottom of the catcher is connected to a flexible 1/4 in. Teflon hose, which drains liquid out of the main chamber and into a collection bottle for recycling. This bottle sits in an ice-bath and is pumped using a mechanical pump in series with a 4 L liquid nitrogen-cooled foreline trap. The collection reservoir pressure is maintained at ~10^{-3} Torr under most conditions.

2.3. Experimental Protocol. Velocities of the molecular beams are determined via time-of-flight (TOF) measurements, using a rotating disk spinning at 200 Hz and containing two narrow slits (16 μs opening) to "chop" a narrow section of the most intense part of the beam. The flight time is measured from the chopper disk to the detector for evaporation experiments, while for scattering experiments, time zero occurs when the most intense part of the molecular beam reaches the interaction region.

Angular distributions from the flat jet were measured from the integrated TOF spectra collected at angles between 0° (parallel to the jet normal) and 90° (parallel to the jet surface) in a back-and-forth manner over four rounds in order to monitor long-term signal instabilities. For each round, the 0° TOF spectrum was measured as a reference, and signal intensities at other angles were normalized accordingly. Overall signal intensities, however, were observed to be rather stable with standard deviations of 3 and 5% for the five 0° spectra of dodecane and Ne evaporation, respectively. Total acquisition times and ionizer emission currents differ between spectra as we always aimed to achieve good signal-to-noise (S/N) ratios, while minimizing the accumulation time and preventing detector saturation. Typical values are 5−15 min acquisition time per spectrum at ionizer emission currents ranging from 0.5 to 3.8 mA.

In the evaporation experiments, neon (99.99% purity) is dissolved in dodecane (n-$C_{12}H_{26}$, TCI America #D0968) by vacuum-degassing the liquid. The degassing process is carried out by simultaneously sonicating and pumping the liquid reservoir using a mechanical pump for 10 min, followed by bubbling noble gas through the liquid until the bottle is pressurized to atmospheric pressure. This procedure was typically repeated five times. We selected Ne as the solute as it is inert and has no internal degrees of freedom, thereby reducing the solute−surface and solute−vapor interactions to physical mechanisms. Moreover, the mass of Ne does not overlap with any solvent ionization fragments produced from dodecane. Dodecane was detected at $m/z = 57$ ($C_4H_9^+$), which represents the butyl cation, a dissociative ionization fragment of dodecane seen at a higher signal intensity than that of the parent ion ($m/z = 170$, $C_{12}H_{26}^+$).[58]

For the scattering experiments, we used pure dodecane flat jets. We produced molecular beams with velocities of 789 ± 44 and 1450 ± 51 m s^{-1} (FWHM) for "slow" Ne (pure) and "fast" Ne (seeded in a 1:9 ratio in He), respectively. The mean translational energies of the incident beam are 6.3 and 21.2 kJ mol^{-1}, respectively. The temporal beam widths are measured to be 65 and 26 μs (FWHM) for slow and fast Ne beams, respectively. In these experiments, θ_i is chosen to be 45, 60, or 80°. TOF spectra are measured without a post-scattering chopper; hence, scattering from the full incident beam profile is collected, but the temporal resolution of the measurement is limited by the duration of the pulsed beam. During data collection for scattering experiments, the background signal in the vacuum chamber is excluded by subtracting "beam-off" data from "beam-on" data.

The flat jet is always caught by a catcher at its first node, and therefore, only the first liquid sheet is exposed (see Figure 1c). A thermocouple is attached onto the stainless-steel chip holder (see Figure 1b) to estimate the liquid temperature inside the holder, T_{holder}, which we assume to be equal to that of the liquid at the chip outlet. The liquid temperature reported in this paper, T_{liq}, is defined as the jet temperature at the detector axis, which is typically 1.5 mm downstream from the tip of the chip for the cylindrical jets and 2 mm downstream for the flat jet. While the cylindrical jet T_{liq} is calculated using the jet temperature equation,[59,60] the flat jet T_{liq} is estimated by using the cylindrical jet temperature equation augmented by an additional term that approximates the ratio of the perimeter to sectional area in order to compensate for the increased evaporative cooling of the flat jet. We estimate the temperature drop $T_{holder} - T_{liq}$, caused by evaporative cooling, to be less than 0.5 °C in our experiment due to the low vapor pressure of dodecane ($P_{vap} = 1.5 \times 10^{-2}$ Torr at 275 K).[61]

3. EXPERIMENTAL RESULTS AND ANALYSIS

3.1. Evaporation. TOF spectra of dodecane and Ne evaporating from flat jets of Ne-doped liquid dodecane are presented in Figure 2 and compared to those of evaporation from cylindrical jets. The detector angle θ_f is defined in Figure 3a. Jet temperatures ranged between T_{liq} = 268 and 291 K and are indicated for each spectrum in the figure caption. Angular distributions for dodecane and Ne evaporating from the flat jet are shown in Figure 3b and are discussed below.

Dodecane evaporation data from a cylindrical jet (Figure 2a, bottom trace) is almost perfectly fitted using a Maxwell−Boltzmann (MB) distribution (blue trace) corresponding to the measured liquid temperature with only a small deviation at longer flight times. The fit indicates that liquid molecules are fully thermalized with the surface liquid when they evaporate.

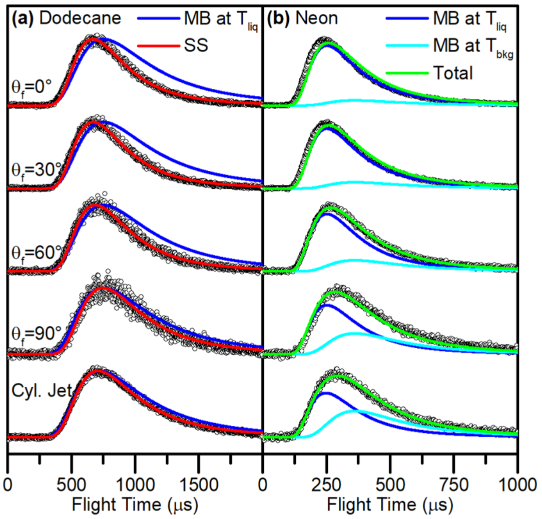

Figure 2. (a) Normalized evaporation TOF spectra of dodecane (detected at $m/z = 57$) from a Ne-doped liquid dodecane flat jet at 268 K and cylindrical jet at 289 K. TOF distributions are fitted using an SS beam distribution (red traces). MB velocity distributions at the liquid temperature (blue traces) are shown for comparison. (b) Normalized evaporation TOF spectra of neon ($m/z = 20$) from a Ne-doped liquid dodecane flat jet at 283 K and a cylindrical jet (bottom) at 291 K. Distributions are fitted using a combination of MB velocity distributions at the liquid temperature (blue traces) and at $T_{\text{bkg}} = 137$ K (light blue traces). The absolute intensity of the T_{bkg} component has been kept constant for all angles. The sum of the two contributions is shown by the green traces.

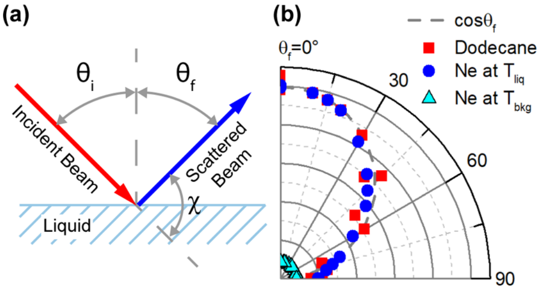

Figure 3. (a) Schematic plot of the scattering geometry. An incident beam (red arrow) is targeted onto the liquid surface (light blue section lines) at the incident angle θ_i. The scattered beam (blue arrow) is detected at the outgoing angle θ_f. (b) Angular plot created from the integrated, non-normalized intensities of the SS (red squares) and MB simulations at T_{liq} and T_{bkg} (blue circles and light blue triangles, respectively) of dodecane and Ne evaporation data at different angles. The cosine function representing the expected angular distribution for evaporation is indicated by the dashed, gray curve.

This scenario is identical to the desorption step of the TD scattering mechanism, assuming that complete thermalization occurs. The MB flux distribution is given by[62]

$$f_{\text{MB}}(v) \propto v^3 \exp\left(-\frac{mv^2}{2RT_{\text{liq}}}\right) \tag{1}$$

where v and m are the velocity and molecular mass of the evaporating molecule, respectively, R is the universal gas constant, and T_{liq} is the liquid temperature.

Dodecane evaporation from the flat jet is shown in the upper traces in Figure 2a for detector angles θ_f of 0, 30, 60, and 90°. The 90° TOF spectrum, which essentially reflects evaporation from the ~50 μm thick jet rims, strongly resembles the MB distribution of the 25 μm cylindrical jet. We estimate that evaporation from the rims contributes <3% to the total flux and is thus negligible at large angles. With decreasing θ_f, the TOF spectra shift toward faster arrival times and become narrower than anticipated for MB evaporation at T_{liq}—the spectra indicate a super-Maxwellian velocity distribution. For dodecane at 0°, the TOF spectrum deviates most significantly from the MB distribution. We also observe a narrowing in our Ne TOF spectra in Figure 2b with decreasing θ_f. However, here, the MB distribution at T_{liq} agrees better with the 0° TOF spectrum, while the 90° spectrum has a noticeably slower and broadened shape. It thus appears that the angle-dependent deviations from an MB distribution in dodecane and Ne evaporation arise from different effects.

We first investigate the super-Maxwellian effect in dodecane evaporation. This phenomenon can be explained by the effect of vapor-phase collisions between evaporating particles above the jet surface that result in acceleration in a manner analogous to supersonic (SS) molecular beam formation.[36] Under these conditions, it is expected that the data will be well-simulated by the flux expression for an SS molecular beam with average flow velocity v_{SS} and average temperature T_{SS}[63,64]

$$f_{\text{SS}}(v) \propto v^3 \exp\left(-\frac{m(v - v_{\text{SS}})^2}{2RT_{\text{SS}}}\right) \tag{2}$$

In the limit of zero collisions, no conversion of thermal motion to flow velocity will occur ($v_{\text{SS}} = 0$ and $T_{\text{SS}} = T_{\text{liq}}$), and $f_{\text{SS}}(v)$ becomes the MB distribution $f_{\text{MB}}(v)$ shown in eq 1. The data in Figure 2a are fitted very well using eq 2 (red traces) for both flat and cylindrical jets. A plot of the fit parameters is presented in Figure 4, where the cylindrical jet data are fit with $v_{\text{SS}} = 73$ m s^{-1} and $T_{\text{SS}} = 210$ K (open circle and square). These values deviate slightly from those for an MB distribution ($v_{\text{SS}} = 0$ and $T_{\text{SS}} = T_{\text{liq}} = 289$ K), suggesting that some collisions occur between the evaporating molecules. In contrast, the flat jet parameters exhibit a considerably larger deviation from the MB distribution. We find that v_{SS} increases from 90 to 135 m s^{-1} with decreasing θ_f, accompanied by a decrease in T_{SS}. Hence, there is considerable thermal relaxation

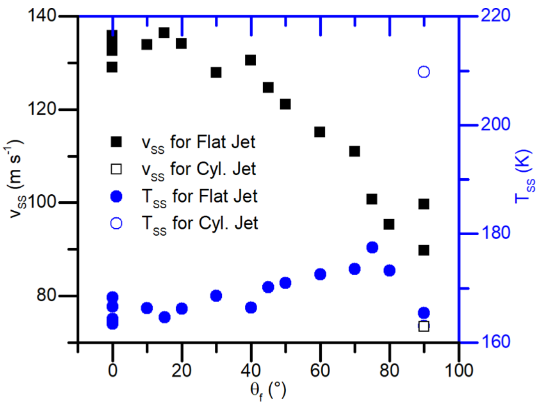

Figure 4. SS beam fit parameters v_{SS} (black squares) and T_{SS} (blue circles) of the velocity distribution of the evaporating dodecane molecules from a flat jet (solid) and a cylindrical jet (open) at different detector angles θ_f. T_{liq} is 268 and 289 K for flat and cylindrical jets, respectively.

analogous to an SS beam expansion, which is most prominent at low θ_f.

The evolution of super-Maxwellian to Maxwellian distributions from $\theta_f = 0°$ to 90° can be understood by the vapor cloud density around the jet. A higher vapor pressure leads to a shorter mean free path λ and therefore a higher collision number N_{coll} for molecules exiting the liquid surface before reaching the detector. One way to describe the trend of N_{coll} is by using the cosine law of evaporation,[65,66] which states that the directional distribution of the evaporating molecules from a flat surface follows a cosθ_f distribution so that there are more collisions at angles closer to the surface normal. Another way to estimate N_{coll} is by using an electrostatic analogy,[60] where the electric field corresponds to the pressure and the electric potential, the integral of the electric field, is analogous to N_{coll}. For example, a flat jet is often simulated by a uniformly charged disk electrode and a cylindrical jet by a charged cylinder. Based on this picture, the evaporative flux decreases with increasing θ_f, similar to how the electric field around a finite disk distorts toward the edges.[67,68] Note that the effective distance from the surface over which collisions take place is large relative to the dimensions of the liquid surface. Thus, the angular-dependent density of the vapor cloud becomes the main consideration when estimating the number of collisions.

To reduce N_{coll}, it is necessary to increase λ, which is inversely proportional to the vapor density and collision cross-section σ. The vapor density is a function of liquid temperature and is limited by the freezing point. However, σ can be reduced by the choice of particles involved. The dodecane−dodecane hard-sphere cross-section has previously been estimated to be ∼250 Å^2[37,69] and is roughly 2 times smaller for Ne−dodecane. In fact, the relative Ne−dodecane cross-section should be even smaller given the omission of van der Waals interactions in the above estimation and considering the very weak interactions between Ne and other species.

In contrast to dodecane evaporation, the TOF spectrum of Ne evaporation at $\theta_f = 0°$ is very well fitted using an MB distribution. Moreover, Ne exhibits TOF distributions that are slower than the MB distribution at high θ_f for T_{liq} (Figure 2b, upper traces). The distribution at $\theta_f = 90°$ deviates significantly, and we are not able to fit it using a single MB distribution. The same observation occurs in the cylindrical jet data (lower trace). Note that using a single SS distribution to fit the cylindrical jet TOF data would result in $T_{SS} = 217$ K and $v_{SS} = 0$ m s^{-1}, which is unrealistic as it would imply that the dramatic decrease in temperature is not accompanied by an increase in the average flow velocity. Additionally, due to the low cross-section of Ne−dodecane, it is unlikely that the distortion of the TOF distribution is caused by vapor collisions. We found that a linear combination of two Maxwellian distributions at T_{liq} (blue trace) and $T_{bkg} = 137$ K (light blue trace) best fits the data. The additional contribution is attributed to Ne evaporating from the cryogenically cooled copper walls, which we measured to be 150 K using a thermocouple. The gradual broadening toward longer arrival times in the Ne TOF spectra with increasing θ_f is thus an artifact of a constant cold Ne background, which contributes more to the total signal as the intensity of Ne evaporating from the jet decreases (owing to the cosθ_f distribution). Other possibilities leading to the additional spectral contribution, such as dodecane fragments or doubly ionized residual argon background, have been systematically addressed and discarded. We observe this effect only for Ne as it is able to escape the cryogenically cooled surface.[70]

To further investigate the origin of the evaporating molecules, we integrate the TOF spectra and plot total intensity as a function of θ_f to yield the angular distributions presented in Figure 3b for dodecane (red squares) and Ne (blue circles). The dodecane data show that the total number of molecules evaporating from a flat surface follows the expected cosθ_f distribution,[66,71,72] highlighting the unique ability of our experiment to measure accurate angular distributions of evaporating volatile liquids.

For Ne evaporation, the two Maxwellian contributions have been integrated separately. Since the TOF spectra in Figure 2b were fitted by assuming a homogeneous Ne background at T_{bkg} in the chamber, this component contributes a constant intensity at all angles (light blue triangles) in Figure 3b. The background-adjusted Ne component (the component at T_{liq}, blue circles) again follows cosθ_f, which further confirms that atoms and molecules with smaller van der Waals radii can escape the dodecane vapor region without undergoing enough gas-phase collisions to significantly distort their angular and velocity distributions. These results suggest that Ne scattering experiments may also be largely unaffected by beam−vapor collisions, a point that is explored in the next section. The slightly super-Maxwellian TOF distribution shape at 0° and the slightly narrowed cosine angular distribution could, however, reflect the interaction potential between Ne and dodecane.[65,73]

3.2. Scattering. Figure 5 shows the TOF spectra for scattering of a fast Ne beam from flat (solid circles) and cylindrical (open circles) dodecane jets. In both cases, the detector is positioned at 90° with respect to the Ne beam. For a cylindrical jet, this corresponds to mean scattering angles of $\theta_i = 33 \pm 22°$ and $\theta_f = 57 \pm 22°$, with the uncertainty attributed to geometric effects.[60] To achieve a direct comparison to the cylindrical jet, the flat jet is rotated to $\theta_i = 33°$. Data acquisition times for the two spectra were the same (∼13 min). The S/N ratio from the flat jet is higher by a factor of 4.4; this represents a ∼20-fold improvement of the acquisition time t as the S/N ratio scales with $\sqrt{t}$. The TOF spectra are fitted using a linear combination of SS and MB distributions, representing IS and TD scattering channels,

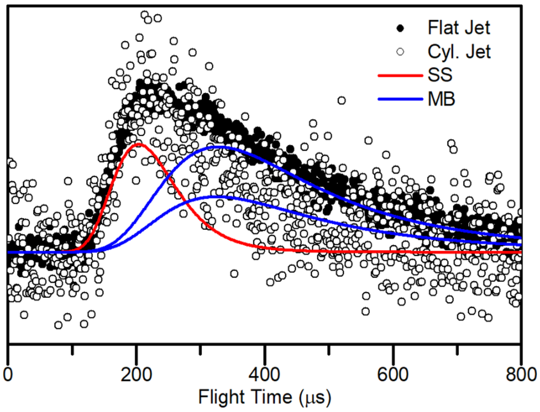

Figure 5. Normalized TOF spectra for scattering of fast Ne atoms from dodecane using a flat liquid jet (solid circles) and a cylindrical liquid jet (open circles). Solid lines show the simulations of the IS component (red trace, SS) and TD components (blue traces, Maxwellian at $T_{liq} = 278$ and 283 K for the flat and cylindrical jet, respectively).

respectively.[74,75] The same SS parameters fit both spectra regardless of the jet type, similar to what was seen for argon scattering off a liquid squalane ($P_{\mathrm{vap}} = 10^{-7}$ Torr at 295 K) cylindrical jet and a wetted wheel,[37] indicating that the measured flat jet scattering signal reflects the interaction between the molecular beam and the liquid surface, rather than with the surrounding vapor sheath.

Our data show more TD for Ne−dodecane scattering compared to the data in ref 37. Our molecular beam was slower with smaller translational energies (6.3 and 21.2 vs 50 kJ mol^{-1}), which increases the energy loss of the incident Ne atom (as we explore later in detail). Thus, the probability of momentarily trapping the incoming gas molecules increases as the gas−surface interaction potential becomes more relevant for small translational energies.

Next, we scattered slow and fast Ne atoms impinging with $\theta_i = 60°$ on a 278 K dodecane flat jet, as shown in Figure 6 for detector angles corresponding to $\theta_f = 30$, 50, 70, and 90°. The molecular beam TOF spectra of the slow and fast beams are shown at the bottom of the two panels. Note that in contrast to the evaporation studies, a chopper wheel is not used in the scattering studies.

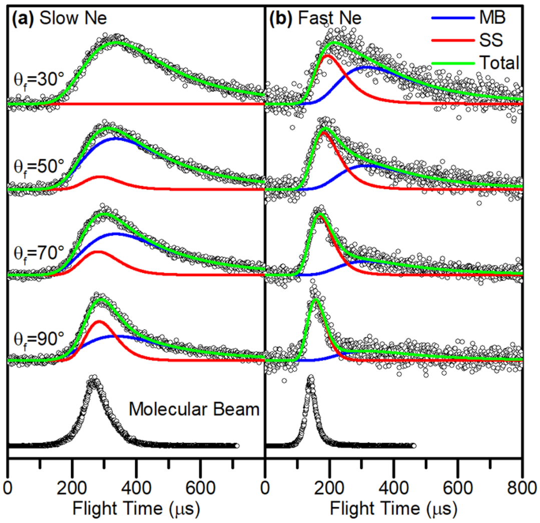

Figure 6. Normalized TOF spectra of (a) slow and (b) fast Ne scattering off a dodecane flat jet with $\theta_i = 60°$. The data are fitted using the sum of an SS distribution (red traces) and an MB distribution at the liquid jet temperature (278 and 277 K for slow and fast Ne, respectively, blue traces). The sum of the two contributions is shown by the green traces. The normalized temporal profiles of the molecular beams are shown at the bottom for reference.

For both Ne beam energies, the scattered TOF spectra vary with θ_f; they become narrower and shift toward faster arrival times as θ_f increases, reflecting a diminished slow component contribution at larger angles. This trend is consistent with the expectation that TD produces a cosθ_f distribution, as was seen in our evaporation data. In fact, by using a two-component fit where an MB distribution and an SS distribution are used for the slow and fast portions of the TOF spectra, respectively, we can readily identify the slower scattered flux arising from TD and the faster scattered flux arising from IS. Note that this fitting procedure involves convolution with the molecular beam temporal profile. As a general trend, we observe a higher IS/TD ratio for the faster Ne beam, meaning that fewer atoms become trapped at the liquid surface.

In order to further characterize these two channels, we plot in Figure 7 the angular dependencies of the integrated TD and IS fits for the slow and fast Ne beams. As expected, the TD components follow a cosine angular distribution, while the IS components are peaked around the 60° specular scattering angle. The fact that the TD contributions closely follow a cosine distribution in all cases indicates at least nearly complete thermal equilibration of the trapped atoms with the liquid surface.

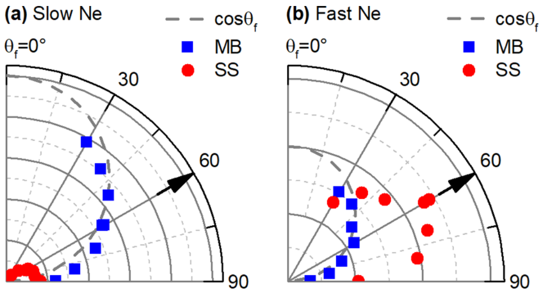

Figure 7. Angular plots created from the integrated, non-normalized intensities of the Ne scattering data at different angles for (a) slow and (b) fast Ne beams. Blue squares represent the TD contributions and red circles the IS contributions to the TOF fits. The cosine function representing the expected angular distribution for evaporation is indicated by the dashed, gray line. Arrows indicate the specular angle.

We also carried out fast Ne scattering at incident angles of 45 and 80°, as shown in Figure 8 with contributions from the IS and TD components indicated. The overall trends remain similar, with the spectra narrowing as θ_f increases. The integrated intensities as a function of scattering angle shown in Figure 9 demonstrate again that the TD component is best approximated by a cosine angular distribution, while the IS component follows a narrow distribution peaked at the specular angle. Moreover, the IS component is clearly larger at the more grazing incidence angle $\theta_i = 80°$.

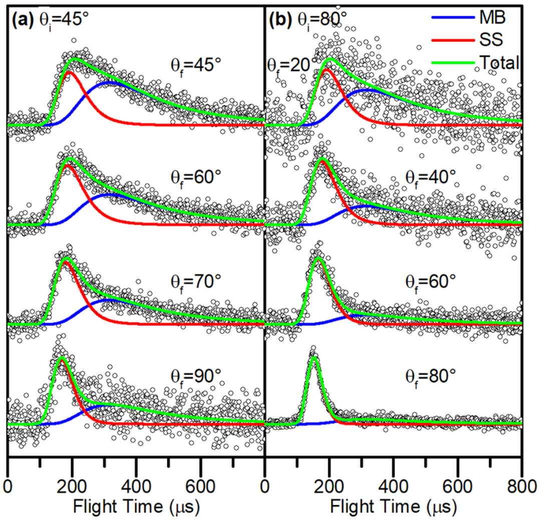

Figure 8. Normalized TOF spectra of fast neon scattering off a dodecane flat jet with (a) $\theta_i = 45°$ and (b) $\theta_i = 80°$, collected by varying θ_f. The data are fitted using the sum of an SS distribution (red traces) and an MB distribution (blue traces) at the liquid jet temperature (276 and 278 K for $\theta_i = 45$ and 80°, respectively). The total fits are shown by the green traces.

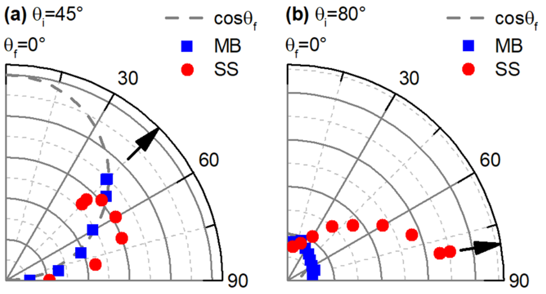

Figure 9. Angular plots created from the integrated, non-normalized intensities of the fast Ne scattering data at different angles for (a) θ_i = 45° and (b) 80°. Blue squares represent the TD contributions and red circles the IS contributions to the TOF fits. The cosine function representing the expected angular distribution for evaporation is indicated by the dashed, gray line. Arrows indicate the specular angle.

The observed trends of increasing IS/TD ratios with increasing θ_f and incident energy agree with the existing literature.[76] These results reflect a higher trapping probability of Ne at the jet surface for smaller collision energies as the gas−surface interaction potential and thermal motion of the surface become more relevant, and sufficient incident energy loss leads to Ne atoms being trapped at the surface. On the other hand, higher energy particles can escape the surface potential energy well more easily. These trapped particles may then undergo thermal equilibration with the liquid and eventually evaporate, leading to an increased TD signal.

Note that the binary IS/TD description provides a powerful way to quantify our observations; however, it may fail under certain circumstances as it does not capture the possible complexity of the scattering mechanism. The breakdown of this simplistic model can be seen in Figures 7a and 9a, where the IS components do not peak at their respective specular angles. This can be explained in the former case by surface roughness, which mediates multiple-bounce collisions, especially occurring for lower collision energies. This holds true in the latter case but is further amplified by a more head-on collision geometry and thus a larger energy transfer.[77]

We next investigate the change in translational energy of the incident Ne beam by analyzing the IS component of the TOF spectra. The average fractional energy loss in the impulsive channel can be described as a function of the deflection angle according to the "soft-sphere" kinematic model[26,78,79]

$$\left(\frac{\Delta E}{E_i}\right) \approx \frac{2\mu}{(1+\mu)^2}\left[1+\mu(\sin\chi)^2 - \cos\chi\sqrt{1-\mu^2(\sin\chi)^2-\frac{E_{\mathrm{int}}}{E_i}(\mu+1)} + \frac{E_{\mathrm{int}}}{E_i}\left(\frac{\mu+1}{2\mu}\right)\right]\left[1+\frac{V-2RT_{\mathrm{liq}}}{E_i}\right] \quad (3)$$

with the absolute change in translational energy $\Delta E = E_i - \langle E_{\mathrm{IS}}\rangle$, incident translational energy E_i, average energy in the IS channel $\langle E_{\mathrm{IS}}\rangle$, mass ratio $\mu = m_{\mathrm{gas}}/m_{\mathrm{eff}}$ of the gas molecule and the effective surface mass, respectively, deflection angle $\chi = 180° - (\theta_i + \theta_f)$, total internal excitation E_{int}, liquid temperature T_{liq}, and gas−surface interaction potential V. It should be noted that since Ne has no internal degrees of freedom, E_{int} only applies to the liquid. This model has been successfully applied to both gas−solid[80] and gas−liquid[78] scattering studies.

Figure 10 plots the calculated translational energy loss as a function of the deflection angle for slow and fast Ne. We observe that an increased energy loss occurs when atoms exit more perpendicularly to the surface (large χ) and the fastest emerging atoms recoil at grazing exit angles (small χ). At θ_i = 60°, the energy loss increases from 10 to 45% between χ = 30 and 90° for fast Ne. For slow Ne, the fractional energy loss ($\Delta E/E_i$) is considerably less, ranging from 0 to 15% over the same range of deflection angles.

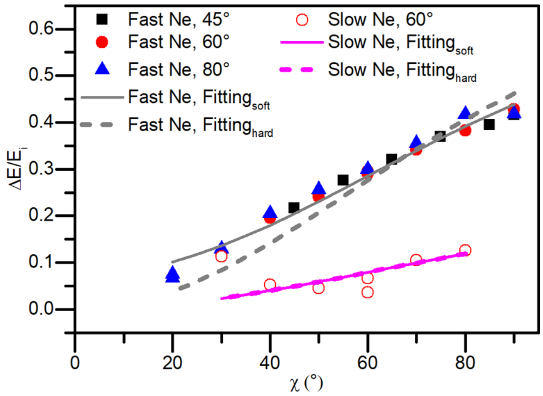

Figure 10. Average fractional energy loss as a function of the deflection angle for impulsively scattered (IS) slow and fast Ne atoms from a dodecane flat jet. Incident translational energies are 6.3 and 21.2 kJ mol^{-1} for slow and fast Ne beams, respectively, and incident angles are indicated in the legend. The solid lines give the predictions of the soft-sphere model, where the incident atom interacts with a localized region of the surface with effective mass, m_{eff}, and this region may increase its internal energy, E_{int}, during collisions. The dashed lines are the predictions of the hard-sphere model where internal excitation has been set to zero. For the slow beam, the soft-sphere and hard-sphere models give indistinguishable predictions. The fitting results for fast and slow Ne using the soft-sphere model are m_{eff} = 62 and 58 amu and E_{int} = 1.9 and 0 kJ mol^{-1}, respectively, whereas the hard-sphere model predicts m_{eff} = 48 and 58 amu, respectively.

Figure 10 also shows fits of eq 3 to the data. While m_{eff} and E_{int} are free parameters, we approximate V = 0 due to the small interaction between Ne and dodecane.[79] For comparison, ab initio calculations of the intermolecular interaction between *n*-pentane(g) and Ne(g) estimate the well depth to be 1.34 kJ mol^{-1},[81] while it is around 11 times deeper for the *n*-pentane dimer (14.9 kJ mol^{-1}).[82] Residuals analysis was then carried out for outlier detection. For slow Ne, the data point at χ = 30° and one of the data points at χ = 60° have been identified as outliers ($p < 0.002$) and thus discarded. For fast Ne, no outliers were determined on the basis of residuals analysis.

Our $\Delta E/E_i$ fitting results yield 62 and 58 amu as the effective surface mass values and E_{int} values of 1.9 and 0 kJ mol^{-1} for fast and slow Ne, respectively. The comparable effective surface masses for slow and fast Ne indicate that the incident gas particles experience a similar "stiffness" of the liquid surface. Similar results have been observed for atomic oxygen scattering from a squalane surface.[78,83] It should be noted that both fitted m_{eff} values are smaller than the dodecane molecular mass, indicating that only part of single dodecane molecule contributes to the scattering during the collision.

The fit results in Figure 10 also show that the soft-sphere model (solid lines) is the correct kinematic model in this case.

https://doi.org/10.1021/acs.jpca.2c01174
J. Phys. Chem. A 2022, 126, 3373−3383

Fitting the "hard-sphere" model with $E_{int} = 0$ in eq 3 provides significantly worse agreement with the fast Ne data, as is indicated by the dashed lines in the figure. This shows that a considerable portion of energy contained in the fast Ne beam is transferred into internal excitation of the liquid. We estimate that 9% of E_i is converted into liquid internal excitation (E_{int}/E_i) for fast Ne, while for slow Ne, nearly no incident energy is dissipated into E_{int} for the IS component.

The kinematic model also provides an explanation for the comparison between cylindrical and flat jet TOF spectra in Figure 5. When fitting the data with the usual two components, we see that the IS channel (red trace) is identical for both setups. This is predicted by the model as the energy loss in the IS channel depends only on χ, rather than independently on θ_i and θ_f. The TD component is larger for the flat jet than for the cylindrical jet at the same incident energy. This effect might arise because cylindrical jet scattering samples larger incident angles, where the TD component is lower in magnitude than at $\theta_i = 33°$.[60]

4. CONCLUSIONS

In this work, a flat liquid jet was incorporated into a crossed molecular beam instrument in order to investigate evaporation and scattering at the gas–liquid interface. Compared to a cylindrical liquid jet, the flat jet offers a considerably larger target area for scattering experiments and the ability to measure well-defined product angular distributions in evaporation and scattering studies. Here, we have reported results on the evaporation of dodecane and Ne from Ne-doped dodecane jets and the scattering of Ne from pure dodecane jets.

In the evaporation experiments, both dodecane and Ne exhibit cosine angular distributions characteristic of TD. TOF measurements show that the dodecane translational energy distributions are "super-Maxwellian" at smaller scattering angles (near the surface normal) and become more "Maxwellian" at larger angles. This effect is attributed to scattering between evaporating molecules, analogous to what happens during an SS expansion. Ne atoms evaporating from the same dodecane surface are fitted well using an MB distribution at all angles once the effects of background scattering from the cryo-cooled chamber walls are accounted for.

Scattering experiments from the surface of dodecane jets were carried out with fast and slow Ne beams. The combination of TOF and angular distributions shows that the scattering could be fit with two components, a faster IS component whose angular distribution peaks at the specular angle and a slower TD component that exhibits a cosine angular distribution. The scattering signals are substantially higher than those from a cylindrical jet under similar conditions, while the translational energy distributions of the two components are the same. The latter result indicates that the translational energy distributions from the flat jet reflect gas–liquid interactions rather than collisions with the vapor surrounding the flat jet. We find that the fast Ne scattering experiments exhibit more IS than TD scattering, consistent with the previous work, and that the IS translational energy distributions show energy transfer to the liquid consistent with a "soft-sphere" kinematic model.

Future experiments will focus on more complex scattering partners and more volatile solvents. We are particularly interested in carrying out evaporation and scattering experiments on flat water jets in order to probe this very important gas–liquid interface and to sort out the effects expected from the increased vapor density surrounding such a jet. These experiments are currently in progress and will be reported soon.

AUTHOR INFORMATION

Corresponding Author

Daniel M. Neumark – *Department of Chemistry, University of California, Berkeley, California 94720, United States; Chemical Sciences Division, Lawrence Berkeley National Laboratory, Berkeley, California 94720, United States;* orcid.org/0000-0002-3762-9473; Email: dneumark@berkeley.edu

Authors

Chin Lee – *Department of Chemistry, University of California, Berkeley, California 94720, United States; Chemical Sciences Division, Lawrence Berkeley National Laboratory, Berkeley, California 94720, United States;* orcid.org/0000-0001-9011-0526

Marvin N. Pohl – *Department of Chemistry, University of California, Berkeley, California 94720, United States; Chemical Sciences Division, Lawrence Berkeley National Laboratory, Berkeley, California 94720, United States;* orcid.org/0000-0002-1790-8440

Isaac A. Ramphal – *Department of Chemistry, University of California, Berkeley, California 94720, United States; Chemical Sciences Division, Lawrence Berkeley National Laboratory, Berkeley, California 94720, United States;* orcid.org/0000-0002-6102-2065

Walt Yang – *Department of Chemistry, University of California, Berkeley, California 94720, United States; Chemical Sciences Division, Lawrence Berkeley National Laboratory, Berkeley, California 94720, United States;* orcid.org/0000-0003-4296-3801

Bernd Winter – *Molecular Physics, Fritz-Haber-Institut der Max-Planck-Gesellschaft, 14195 Berlin, Germany;* orcid.org/0000-0002-5597-8888

Bernd Abel – *Department of Functional Surfaces, Leibniz Institute of Surface Engineering (IOM), 04318 Leipzig, Germany; Wilhelm-Ostwald-Institute for Physical and Theoretical Chemistry, University of Leipzig, 04318 Leipzig, Germany;* orcid.org/0000-0001-6032-1680

Complete contact information is available at: https://pubs.acs.org/10.1021/acs.jpca.2c01174

Author Contributions

[#]C.L. and M.N.P. contributed equally.

Notes

The authors declare no competing financial interest.

ACKNOWLEDGMENTS

C.L., M.N.P., I.A.R., W.Y., and D.M.N. acknowledge the support by the Office of Basic Energy Science, Chemical Sciences Division of the U.S. Department of Energy under Contract no. DE-AC02-05CH11231. C.L., M.N.P., I.A.R., W.Y., and D.M.N. thank Daniel P. DePonte for useful discussions regarding the chip design. M.N.P. acknowledges additional support from the Alexander von Humboldt Foundation. B.W. acknowledges support from the German Research Foundation (Wi 1327/5−1). B.A. thanks the Miller Institute of UC Berkeley for support through the Somorjai

Miller Guest Professorship Award and the German Research Foundation for funding (AB63/19−1). This research used the resources of the SLAC National Accelerator Laboratory, supported by the U.S. Department of Energy, Office of Science, Office of Basic Energy Sciences under Contract no. DE-AC02-76SF00515.

■ REFERENCES

(1) Wallington, T. J.; Kaiser, E. W.; Farrell, J. T. Automotive fuels and internal combustion engines: a chemical perspective. *Chem. Soc. Rev.* **2006**, *35*, 335−347.

(2) Singh, A.; Agrawal, M. Acid rain and its ecological consequences. *J. Environ. Biol.* **2008**, *29*, 15−24.

(3) Putikam, R.; Lin, M.-C. A novel mechanism for the isomerization of N_2O_4 and its implication for the reaction with H_2O and acid rain formation. *Int. J. Quantum Chem.* **2018**, *118*, e25560.

(4) Ruiz-López, M. F.; Martins-Costa, M. T. C.; Anglada, J. M.; Francisco, J. S. A New Mechanism of Acid Rain Generation from HOSO at the Air-Water Interface. *J. Am. Chem. Soc.* **2019**, *141*, 16564−16568.

(5) Valsaraj, K. T. A Review of the Aqueous Aerosol Surface Chemistry in the Atmospheric Context. *Open J. Phys. Chem.* **2012**, *2*, 58−66.

(6) Sabine, C. L.; Feely, R. A.; Gruber, N.; Key, R. M.; Lee, K.; Bullister, J. L.; Wanninkhof, R.; Wong, C. S.; Wallace, D. W. R.; Tilbrook, B.; et al. The Oceanic Sink for Anthropogenic CO_2. *Science* **2004**, *305*, 367−371.

(7) Finlayson-Pitts, B. J.; Pitts, J. N. *Chemistry of the Upper and Lower Atmosphere: Theory, Experiments, and Applications*; Academic Press: San Diego, 2000.

(8) Jungwirth, P.; Tobias, D. J. Specific Ion Effects at the Air/Water Interface. *Chem. Rev.* **2006**, *106*, 1259−1281.

(9) Ahmed, M.; Blum, M.; Crumlin, E. J.; Geissler, P. L.; Head-Gordon, T.; Limmer, D. T.; Mandadapu, K. K.; Saykally, R. J.; Wilson, K. R. Molecular Properties and Chemical Transformations Near Interfaces. *J. Phys. Chem. B* **2021**, *125*, 9037−9051.

(10) Richmond, G. L. Molecular Bonding and Interactions at Aqueous Surfaces as Probed by Vibrational Sum Frequency Spectroscopy. *Chem. Rev.* **2002**, *102*, 2693−2724.

(11) McGuire, J. A.; Shen, Y. R. Ultrafast Vibrational Dynamics at Water Interfaces. *Science* **2006**, *313*, 1945−1948.

(12) Petersen, P. B.; Saykally, R. J. On the nature of ions at the liquid water surface. *Annu. Rev. Phys. Chem.* **2006**, *57*, 333−364.

(13) Thürmer, S.; Seidel, R.; Faubel, M.; Eberhardt, W.; Hemminger, J. C.; Bradforth, S. E.; Winter, B. Photoelectron Angular Distributions from Liquid Water: Effects of Electron Scattering. *Phys. Rev. Lett.* **2013**, *111*, 173005.

(14) Suzuki, Y. I.; Nishizawa, K.; Kurahashi, N.; Suzuki, T. Effective attenuation length of an electron in liquid water between 10 and 600 eV. *Phys. Rev. E: Stat., Nonlinear, Soft Matter Phys.* **2014**, *90*, 010302.

(15) Signorell, R. Electron Scattering in Liquid Water and Amorphous Ice: A Striking Resemblance. *Phys. Rev. Lett.* **2020**, *124*, 205501.

(16) Artiglia, L.; Edebeli, J.; Orlando, F.; Chen, S.; Lee, M.-T.; Corral Arroyo, P.; Gilgen, A.; Bartels-Rausch, T.; Kleibert, A.; Vazdar, M.; et al. A surface-stabilized ozonide triggers bromide oxidation at the aqueous solution-vapour interface. *Nat. Commun.* **2017**, *8*, 700.

(17) Ghosal, S.; Hemminger, J. C.; Bluhm, H.; Mun, B. S.; Hebenstreit, E. L. D.; Ketteler, G.; Ogletree, D. F.; Requejo, F. G.; Salmeron, M. Electron Spectroscopy of Aqueous Solution Interfaces Reveals Surface Enhancement of Halides. *Science* **2005**, *307*, 563−566.

(18) Kappes, K. J.; Deal, A. M.; Jespersen, M. F.; Blair, S. L.; Doussin, J.-F.; Cazaunau, M.; Pangui, E.; Hopper, B. N.; Johnson, M. S.; Vaida, V. Chemistry and Photochemistry of Pyruvic Acid at the Air-Water Interface. *J. Phys. Chem. A* **2021**, *125*, 1036−1049.

(19) Li, Y.; Yan, X.; Cooks, R. G. The Role of the Interface in Thin Film and Droplet Accelerated Reactions Studied by Competitive Substituent Effects. *Angew. Chem., Int. Ed.* **2016**, *55*, 3433−3437.

(20) Nam, I.; Lee, J. K.; Nam, H. G.; Zare, R. N. Abiotic production of sugar phosphates and uridine ribonudeoside in aqueous microdroplets. *Proc. Natl. Acad. Sci. U.S.A.* **2017**, *114*, 12396−12400.

(21) Diveky, M. E.; Gleichweit, M. J.; Roy, S.; Signorell, R. Shining New Light on the Kinetics of Water Uptake by Organic Aerosol Particles. *J. Phys. Chem. A* **2021**, *125*, 3528−3548.

(22) Neumark, D. M.; Wodtke, A. M.; Robinson, G. N.; Hayden, C. C.; Lee, Y. T. Molecular beam studies of the F+H_2 reaction. *J. Chem. Phys.* **1985**, *82*, 3045−3066.

(23) Continetti, R. E.; Balko, B. A.; Lee, Y. T. Crossed molecular beams study of the reaction D+H_2→DH+H at collision energies of 0.53 and 1.01 eV. *J. Chem. Phys.* **1990**, *93*, 5719−5740.

(24) Weinberg, W. H. Molecular beam scattering from solid surfaces. *Adv. Colloid Interface Sci.* **1975**, *4*, 301−347.

(25) Cardillo, M. J. Molecular beam scattering from solid surfaces: He diffraction, hyperthermal scattering, and surface dynamics. *Surf. Sci.* **1994**, *299*, 277−283.

(26) Nathanson, G. M. Molecular beam studies of gas-liquid interfaces. *Annu. Rev. Phys. Chem.* **2004**, *55*, 231−255.

(27) Kinefuchi, I.; Yamaguchi, H.; Shiozaki, S.; Sakiyama, Y.; Matsumoto, Y. Out-of-plane Scattering Distribution of Nitrogen Molecular Beam on Graphite (0001) Surface. *AIP Conf. Proc.* **2005**, *762*, 947−952.

(28) Lednovich, S. L.; Fenn, J. B. Absolute Evaporation Rates for Some Polar and Nonpolar Liquids. *AIChE J.* **1977**, *23*, 454−459.

(29) Siegbahn, H. Electron Spectroscopy for Chemical Analysis of Liquids and Solutions. *J. Phys. Chem.* **1985**, *89*, 897−909.

(30) King, M. E.; Nathanson, G. M.; Hanning-Lee, M.; Minton, T. K. Probing the Microscopic Corrugation of Liquid Surfaces with Gas-Liquid Collisions. *Phys. Rev. Lett.* **1993**, *70*, 1026−1029.

(31) Nathanson, G. M.; Davidovits, P.; Worsnop, D. R.; Kolb, C. E. Dynamics and Kinetics at the Gas-Liquid Interface. *J. Phys. Chem.* **1996**, *100*, 13007−13020.

(32) Wu, B.; Zhang, J.; Minton, T. K.; McKendrick, K. G.; Slattery, J. M.; Yockel, S.; Schatz, G. C. Scattering Dynamics of Hyperthermal Oxygen Atoms on Ionic Liquid Surfaces: [emim][NTf_2] and [C_{12}mim][NTf_2]. *J. Phys. Chem. C* **2010**, *114*, 4015−4027.

(33) Brastad, S. M.; Nathanson, G. M. Molecular beam studies of HCl dissolution and dissociation in cold salty water. *Phys. Chem. Chem. Phys.* **2011**, *13*, 8284−8295.

(34) Lane, P. D.; Moncrieff, K. E.; Greaves, S. J.; McKendrick, K. G.; Costen, M. L. Inelastic Scattering of CN Radicals at the Gas-Liquid Interface Probed by Frequency-Modulated Absorption Spectroscopy. *J. Phys. Chem. C* **2020**, *124*, 16439−16448.

(35) Faubel, M.; Schlemmer, S.; Toennies, J. P. A molecular beam study of the evaporation of water from a liquid jet. *ZPhys-e.D: At., Mol. Clusters* **1988**, *10*, 269−277.

(36) Faubel, M.; Kisters, T. Non-equilibrium molecular evaporation of carboxylic acid dimers. *Nature* **1989**, *339*, 527−529.

(37) Lancaster, D. K.; Johnson, A. M.; Burden, D. K.; Wiens, J. P.; Nathanson, G. M. Inert Gas Scattering from Liquid Hydrocarbon Microjets. *J. Phys. Chem. Lett.* **2013**, *4*, 3045−3049.

(38) Faust, J. A.; Sobyra, T. B.; Nathanson, G. M. Gas-Microjet Reactive Scattering: Collisions of HCl and DCl with Cool Salty Water. *J. Phys. Chem. Lett.* **2016**, *7*, 730−735.

(39) Gord, J. R.; Zhao, X.; Liu, E.; Bertram, T. H.; Nathanson, G. M. Control of Interfacial Cl_2 and N_2O_5 Reactivity by a Zwitterionic Phospholipid in Comparison with Ionic and Uncharged Surfactants. *J. Phys. Chem. A* **2018**, *122*, 6593−6604.

(40) Shaloski, M. A.; Gord, J. R.; Staudt, S.; Quinn, S. L.; Bertram, T. H.; Nathanson, G. M. Reactions of N_2O_5 with Salty and Surfactant-Coated Glycerol: Interfacial Conversion of Br^- to Br_2 Mediated by Alkylammonium Cations. *J. Phys. Chem. A* **2017**, *121*, 3708−3719.

(41) Sobyra, T. B.; Melvin, M. P.; Nathanson, G. M. Liquid Microjet Measurements of the Entry of Organic Acids and Bases into Salty Water. *J. Phys. Chem. C* **2017**, *121*, 20911−20924.

(42) Ekimova, M.; Quevedo, W.; Faubel, M.; Wernet, P.; Nibbering, E. T. J. A liquid flatjet system for solution phase soft-x-ray spectroscopy. *Struct. Dyn.* **2015**, *2*, 054301.

(43) Luu, T. T.; Yin, Z.; Jain, A.; Gaumnitz, T.; Pertot, Y.; Ma, J.; Wörner, H. J. Extreme-ultraviolet high-harmonic generation in liquids. *Nat. Commun.* **2018**, *9*, 3723.

(44) Menzi, S.; Knopp, G.; Al Haddad, A.; Augustin, S.; Borca, C.; Gashi, D.; Huthwelker, T.; James, D.; Jin, J.; Pamfilidis, G.; et al. Generation and simple characterization of flat, liquid jets. *Rev. Sci. Instrum.* **2020**, *91*, 105109.

(45) Tcypkin, A. N.; Ponomareva, E. A.; Putilin, S. E.; Smirnov, S. V.; Shtumpf, S. A.; Melnik, M. V.; E, Y.; Kozlov, S. A.; Zhang, X.-C. Flat liquid jet as a highly efficient source of terahertz radiation. *Opt. Express* **2019**, *27*, 15485−15494.

(46) Malerz, S.; Haak, H.; Trinter, F.; Stephansen, A. B.; Kolbeck, C.; Pohl, M.; Hergenhahn, U.; Meijer, G.; Winter, B. A setup for studies of photoelectron circular dichroism from chiral molecules in aqueous solution. *Rev. Sci. Instrum.* **2022**, *93*, 015101.

(47) Edwards, T.; Maurice, L. Q. Surrogate Mixtures to Represent Complex Aviation and Rocket Fuels. *J. Propul. Power* **2001**, *17*, 461−466.

(48) Lee, Y. T.; Mcdonald, J. D.; Lebreton, P. R.; Herschbach, D. R. Molecular Beam Reactive Scattering Apparatus with Electron Bombardment Detector. *Rev. Sci. Instrum.* **1969**, *40*, 1402−1408.

(49) Lee, Y. T. Molecular Beam Studies of Elementary Chemical Processes (Nobel Lecture). *Angew. Chem., Int. Ed.* **1987**, *26*, 939−951.

(50) Irimia, D.; Dobrikov, D.; Kortekaas, R.; Voet, H.; van den Ende, D. A.; Groen, W. A.; Janssen, M. H. M. A short pulse (7 μs FWHM) and high repetition rate (dc-5kHz) cantilever piezovalve for pulsed atomic and molecular beams. *Rev. Sci. Instrum.* **2009**, *80*, 113303.

(51) Meng, C.; Janssen, M. H. M. Measurement of the density profile of pure and seeded molecular beams by femtosecond ion imaging. *Rev. Sci. Instrum.* **2015**, *86*, 023110.

(52) *Fundamentals of Vacuum Technology*; Umrath, W., Eds.; Oerlikon Leybold Vacuum: Cologne, Germany, 2007.

(53) Charvat, A.; Lugovoj, E.; Faubel, M.; Abel, B. New design for a time-of-flight mass spectrometer with a liquid beam laser desorption ion source for the analysis of biomolecules. *Rev. Sci. Instrum.* **2004**, *75*, 1209−1218.

(54) Bush, J. W. M.; Hasha, A. E. On the collision of laminar jets: fluid chains and fishbones. *J. Fluid Mech.* **2004**, *511*, 285−310.

(55) Bremond, N.; Villermaux, E. Atomization by jet impact. *J. Fluid Mech.* **2006**, *549*, 273−306.

(56) Koralek, J. D.; Kim, J. B.; Brůža, P.; Curry, C. B.; Chen, Z.; Bechtel, H. A.; Cordones, A. A.; Sperling, P.; Toleikis, S.; Kern, J. F.; et al. Generation and characterization of ultrathin free-flowing liquid sheets. *Nat. Commun.* **2018**, *9*, 1353.

(57) Winter, B. Liquid microjet for photoelectron spectroscopy. *Nucl. Instrum. Methods Phys. Res., Sect. A* **2009**, *601*, 139−150.

(58) NIST Mass Spectrometry Data Center, Wallace, W. E. Mass Spectra. In *NIST Chemistry WebBook, NIST Standard Reference Database 69 [Online]*; Linstrom, P. J., Mallard, W. G., Eds.; National Institute of Standards and Technology: Gaithersburg MD, 20899, 2014. (accessed February 14, 2022).

(59) Cappa, C. D.; Drisdell, W. S.; Smith, J. D.; Saykally, R. J.; Cohen, R. C. Isotope Fractionation of Water during Evaporation without Condensation. *J. Phys. Chem. B* **2005**, *109*, 24391−24400.

(60) Faust, J. A.; Nathanson, G. M. Microjets and coated wheels: versatile tools for exploring collisions and reactions at gas-liquid interfaces. *Chem. Soc. Rev.* **2016**, *45*, 3609−3620.

(61) Sasse, K.; Jose, J.; Merlin, J.-C. A static apparatus for measurement of low vapor pressures. Experimental results on high molecular-weight hydrocarbons. *Fluid Phase Equilib.* **1988**, *42*, 287−304.

(62) Comsa, G.; David, R. Dynamical parameters of desorbing molecules. *Surf. Sci. Rep.* **1985**, *5*, 145−198.

(63) Lebehot, A.; Kurzyna, J.; Lago, V.; Dudeck, M.; Campargue, R. In *Atomic and Molecular Beams*; Campargue, R., Ed.; Springer: New York, 2001; pp 237−251.

(64) Morse, M. D. In *Atomic, Molecular, and Optical Physics: Atoms and Molecules*; Dunning, F. B., Hulet, R. G., Eds.; Academic Press: San Diego, California, 1996; Vol. *29B*, pp 21−47.

(65) Kann, Z. R.; Skinner, J. L. Sub- and super-Maxwellian evaporation of simple gases from liquid water. *J. Chem. Phys.* **2016**, *144*, 154701.

(66) Kennard, E. H. *Kinetic Theory of Gases*; McGraw-Hill Book Company: New York, 1938.

(67) Bochko, V.; Silagadze, Z. K. On the electrostatic potential and electric field of a uniformly charged disk. *Eur. J. Phys.* **2020**, *41*, 045201.

(68) Purcell, E. M.; Morin, D. J. *Electricity and Magnetism*; Cambridge University Press: New York, 2013.

(69) Cummings, G. A. M.; Ubbelohde, A. R. Collision Diameters of Flexible Hydrocarbon Molecules in the Vapour Phase: The "Hydrogen Effect". *J. Chem. Soc.* **1953**, 3751−3755.

(70) Day, C. In *CAS—CERN Accelerator School: Vacuum in Accelerators*; Brandt, D., Ed.; CERN: Geneva, Switzerland, 2007; pp 241−274.

(71) Garton, D. J.; Minton, T. K.; Alagia, M.; Balucani, N.; Casavecchia, P.; Gualberto Volpi, G. Comparative dynamics of Cl(^2P) and O(^3P) interactions with a hydrocarbon surface. *J. Chem. Phys.* **2000**, *112*, 5975−5984.

(72) King, M. E.; Fiehrer, K. M.; Nathanson, G. M.; Minton, T. K. Effects of Thermal Roughening on the Angular Distributions of Trapping and Scattering in Gas-Liquid Collisions. *J. Phys. Chem. A* **1997**, *101*, 6556−6561.

(73) Patel, E.-H.; Williams, M. A.; Koehler, S. P. K. Kinetic Energy and Angular Distributions of He and Ar Atoms Evaporating from Liquid Dodecane. *J. Phys. Chem. B* **2017**, *121*, 233−239.

(74) Saecker, M. E.; Govoni, S. T.; Kowalski, D. V.; King, M. E.; Nathanson, G. M. Molecular Beam Scattering from Liquid Surfaces. *Science* **1991**, *252*, 1421−1424.

(75) Kinefuchi, I.; Kotsubo, Y.; Osuka, K.; Yoshimoto, Y.; Miyoshi, N.; Takagi, S.; Matsumoto, Y. Incident energy dependence of the scattering dynamics of water molecules on silicon and graphite surfaces: the effect on tangential momentum accommodation. *Microfluid. Nanofluid.* **2017**, *21*, 15.

(76) Headgordon, M.; Tully, J. C.; Rettner, C. T.; Mullins, C. B.; Auerbach, D. J. On the nature of trapping and desorption at high surface temperatures. Theory and experiments for the Ar-Pt(111) system. *J. Chem. Phys.* **1991**, *94*, 1516−1527.

(77) Tesa-Serrate, M. A.; Smoll, E. J.; Minton, T. K.; McKendrick, K. G. Atomic and Molecular Collisions at Liquid Surfaces. *Annu. Rev. Phys. Chem.* **2016**, *67*, 515−540.

(78) Alexander, W. A.; Zhang, J.; Murray, V. J.; Nathanson, G. M.; Minton, T. K. Kinematics and dynamics of atomic-beam scattering on liquid and self-assembled monolayer surfaces. *Faraday Discuss.* **2012**, *157*, 355−374.

(79) Rettner, C. T.; Ashfold, M. N. R. In *Dynamics of Gas-Surface Interactions*; Royal Society of Chemistry: Cambridge, 1991.

(80) Andric, N.; Jenny, P. Molecular dynamics investigation of energy transfer during gas-surface collisions. *Phys. Fluids* **2018**, *30*, 077104.

(81) Balabin, R. M. Intermolecular dispersion interactions of normal alkanes with rare gas atoms: van der Waals complexes of n-pentane with helium, neon, and argon. *Chem. Phys.* **2008**, *352*, 267−275.

(82) Tsuzuki, S.; Honda, K.; Uchimaru, T.; Mikami, M. Magnitude of Interaction between *n*-Alkane Chains and Its Anisotropy: High-Level ab Initio Calculations of *n*-Butane, *n*-Petane, and *n*-Hexane Dimers. *J. Phys. Chem. A* **2004**, *108*, 10311−10316.

(83) Zhang, J.; Garton, D. J.; Minton, T. K. Reactive and inelastic scattering dynamics of hyperthermal oxygen atoms on a saturated hydrocarbon surface. *J. Chem. Phys.* **2002**, *117*, 6239−6251.